Arch. Metall. Mater. **65** (2020), 4, 1249-1254

DOI: 10.24425/amm.2020.133678

JUNHYUB JEON[1], SEUNGGYU CHOI[1], NAMHYUK SEO[1],
YOUNG HOON MOON[2], IN-JIN SHON[1], SEOK-JAE LEE[1*]

EFFECTS OF TiC ADDITION ON STRAIN-INDUCED MARTENSITE TRANSFORMATION AND MECHANICAL PROPERTIES OF NANOCRYSTALLINE Fe-Mn ALLOY FABRICATED BY SPARK PLASMA SINTERING

The effect of TiC content on the microstructure and mechanical properties of a nanocrystalline Fe-Mn alloy was investigated by XRD analysis, TEM observation, and mechanical tests. A sintered Fe-Mn alloy sample with nano-sized crystallites was obtained using spark plasma sintering. Crystallite size, which is used as a hardening mechanism, was measured by X-ray diffraction peak analysis. It was observed that the addition of TiC influenced the average size of crystallites, resulting in a change in austenite stability. Thus, the volume fraction of austenite at room temperature after the sintering process was also modified by the TiC addition. The martensite transformation during cooling was suppressed by adding TiC, which lowered the martensite start temperature. The plastic behavior and the strain-induced martensite kinetics formed during plastic deformation are discussed with compressive stress-strain curves and numerical analysis for the transformation kinetics.

Keywords: Fe-Mn alloy, ceramic reinforcement, austenite stability, mechanical properties, spark plasma sintering

1. Introduction

In recent years, reducing CO_2 emission of automobiles has become a pressing environmental issue due to its destructive impact on global warming [1,2]. About 20% of total CO_2 emissions in the world originate from various forms of transportation, while approximately 70% of them are caused by automobiles. The most effective solution is to reduce the weight of automobiles by using new stronger materials. This is why many researchers over the past decade have devoted themselves to the development of third-generation advanced high strength steel (AHSS).

Transformation-induced plasticity (TRIP) plays an important role in achieving better mechanical properties. In conventional processes, intercritical annealing is performed on cold-rolled sheet steel, generating a certain amount of retained austenite at room temperature. In binary Fe-X alloy diagrams, the fcc austenite phase is stable above Ae3 temperature, but retained austenite at room temperature is in a metastable phase. This means that this metastable phase can be transformed into a stable phase by applying external deformation or heat treatment. When the material containing retained austenite at room temperature is plastically deformed, austenite constantly transforms into strain-induced martensite, depending on the strain. The transformed strain-induced martensite contributes both to improved strength and ductility [3,4].

The transformation kinetics of strain-induced martensite are originally controlled by the austenite stability of. As previously reported, several factors influence austenite stability, including chemical composition [5-9], grain size [10-13], mechanical stabilization [14,15]. Most previous studies have focused on the relationship between the aforementioned factors, microstructure, and mechanical properties in third-generation AHSS produced by conventional processes [5,6,15]. However, several studies have been conducted to investigate the TRIP effect in sintered alloy steels prepared by powder metallurgy. Recently, some studies have reported regarding the transformation kinetics of strain-induced martensite in Fe-Mn [16-19] or Fe-Ni [20,21] alloys fabricated by powder metallurgy. These previous studies have mainly focused on strengthening mechanisms related to solid solution, grain refinement, and martensite hardening. Taking all these factors into account, then, the present study, investigated the effects of TiC precipitate particles on austenite stability, as well as the transformation kinetics of strain-induced martensite in an Fe-7%Mn alloy fabricated by powder metallurgy.

[1] JEONBUK NATIONAL UNIVERSITY, DIVISION OF ADVANCED MATERIALS ENGINEERING, 567 BAEKJE-DAERO, DEOKJIN-GU, JEONJU, 54896, REPUBLIC OF KOREA
[2] PUSAN NATIONAL UNIVERSITY, SCHOOL OF MECHANICAL ENGINEERING, 2, BUSANDAEHAK-RO 63BEON-GIL, GEUMJEONG-GU, BUSAN, 46241, REPUBLIC OF KOREA

* Corresponding author: seokjaelee@jbnu.ac.kr

2. Experimental

Fe-7%Mn and Fe-7%Mn-6%TiC alloys (in wt.%) were designed in this study. Fe powder with a purity of 99.9% and average particle size of <75 μm, Mn powder with a purity of 99.6% and average particle size of <20 μm, and TiC powder with a purity of 98% and average particle size of 100 nm were mechanically alloyed using a high-energy ball mill (a Pulverisette-5 planetary mill) at 250 rpm for 24 h. Tungsten carbide balls with a diameter of 10 mm were used for milling in a sealed cylindrical SKD-11 tool steel jar, with a ball to powder ratio of 30:1 under argon atmosphere. Spark plasma sintering (SPS) was adopted to fabricate sintered samples. The milled alloy powders were poured into a cylindrical graphite die with an inner diameter of 10 mm, an outer diameter of 35 mm, and a height of 40 mm. Two graphite punches with a diameter of 10 mm and a height of 20 mm were used to seal the graphite die. The milled alloy powders were heated to 1000°C at a heating rate of 1000°C/min under a high vacuum condition of below 150 mtorr, then immediately cooled to room temperature in a vacuum chamber. A uniaxial pressure of about 88 MPa was applied while sintering. Small specimens with a diameter of 4 mm were machined by wire electric discharge machining from the sintered samples. A compressive test was carried out using a universal testing machine (Instron 5569) with a strain rate of 1×10^{-3} s^{-1}. Hardness measurement of the sintered specimens was conducted using a Rockwell hardness tester (SSAUL BESTECH, BESTROC-300N). Microstructural features of the specimens were analyzed with X-ray diffraction (XRD, RIGAKU, MAX-2500), electron backscatter diffraction (EBSD) using a field emission scanning electron microscope (FE-SEM, ZEISS, Merlin Compact) and scanning transmission electron microscopy (STEM, JEOL, JEM-ARM200F). The TEM specimen was fabricated using a focused ion beam (FIB, JEOL, JIB-4601F).

3. Results and discussion

Fig. 1 shows the XRD results for the milled powders. Whereas only bcc α-Fe peaks appeared in the milled Fe-7%Mn powder, bcc α-Fe peaks with some peaks of TiC appeared in the milled Fe-7%Mn-6%TiC powder. No peak for Mn was observed since Mn atoms were mechanically alloyed in the Fe matrix. However, TiC peaks were confirmed because TiC particles were not dissolved by the high energy ball mill and dispersed in the Fe matrix as initial carbides in the milled Fe-7%-6%TiC powder. The crystallite size of the milled powder was calculated using the following equation [22].

$$\beta \cdot \cos\theta = \frac{k \cdot \lambda}{D} + 4\varepsilon \cdot \sin\theta \tag{1}$$

where β is the full width at half maximum (FWHM) of XRD peaks, θ is the Bragg angle, k is the constant, λ is the wavelength of Cu Kα target (= 1.5406 Å), D is the crystallite size, and ε is the strain. The crystallite sizes of the milled Fe-7%Mn and Fe-7%Mn-6%TiC powders were calculated as 12 nm and 10 nm respectively. The addition of TiC resulted in a slight decrease in crystallite size in the milled Fe-7%Mn powder.

Fig. 2 shows the XRD results for the as-sintered and deformed specimens. The existence of fcc γ-Fe peaks was confirmed, while no fcc γ-Fe peak was observed in the raw powders, as seen in Fig. 1. The austenite phase (fcc γ-Fe) was transformed during heating and a certain amount of austenite remained at room temperature after the SPS. The TiC peaks were still apparent in the sintered and deformed Fe-7%Mn-6%TiC specimens. The volume fraction of austenite was calculated using the following equation [23].

$$V_\gamma = \frac{\dfrac{I_{\gamma(200)} + I_{\gamma(220)} + I_{\gamma(311)}}{3}}{\dfrac{I_{\alpha(200)} + I_{\alpha(211)}}{2} + \dfrac{I_{\gamma(200)} + I_{\gamma(220)} + I_{\gamma(311)}}{3}} \tag{2}$$

where V_γ is the austenite volume fraction and I_γ and I_α are the intensity of austenite and ferrite peaks. The volume fractions of austenite for the as-sintered Fe-7%Mn and Fe-7%Mn-6%TiC specimens were 71.10 and 75.59 vol.% respectively. It is believed that slightly smaller crystallite size of 10 nm for Fe-7%Mn-6%TiC alloy contributes to increased austenite stability, resulting in a higher volume fraction of austenite after sintering.

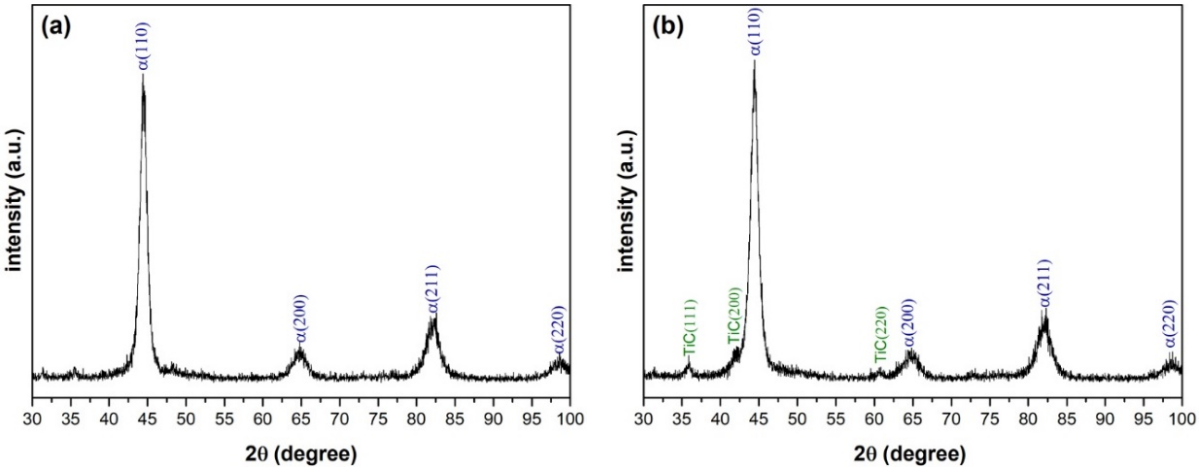

Fig. 1. XRD patterns of the milled powders: (a) Fe-7%Mn and (b) Fe-7%Mn-6%TiC

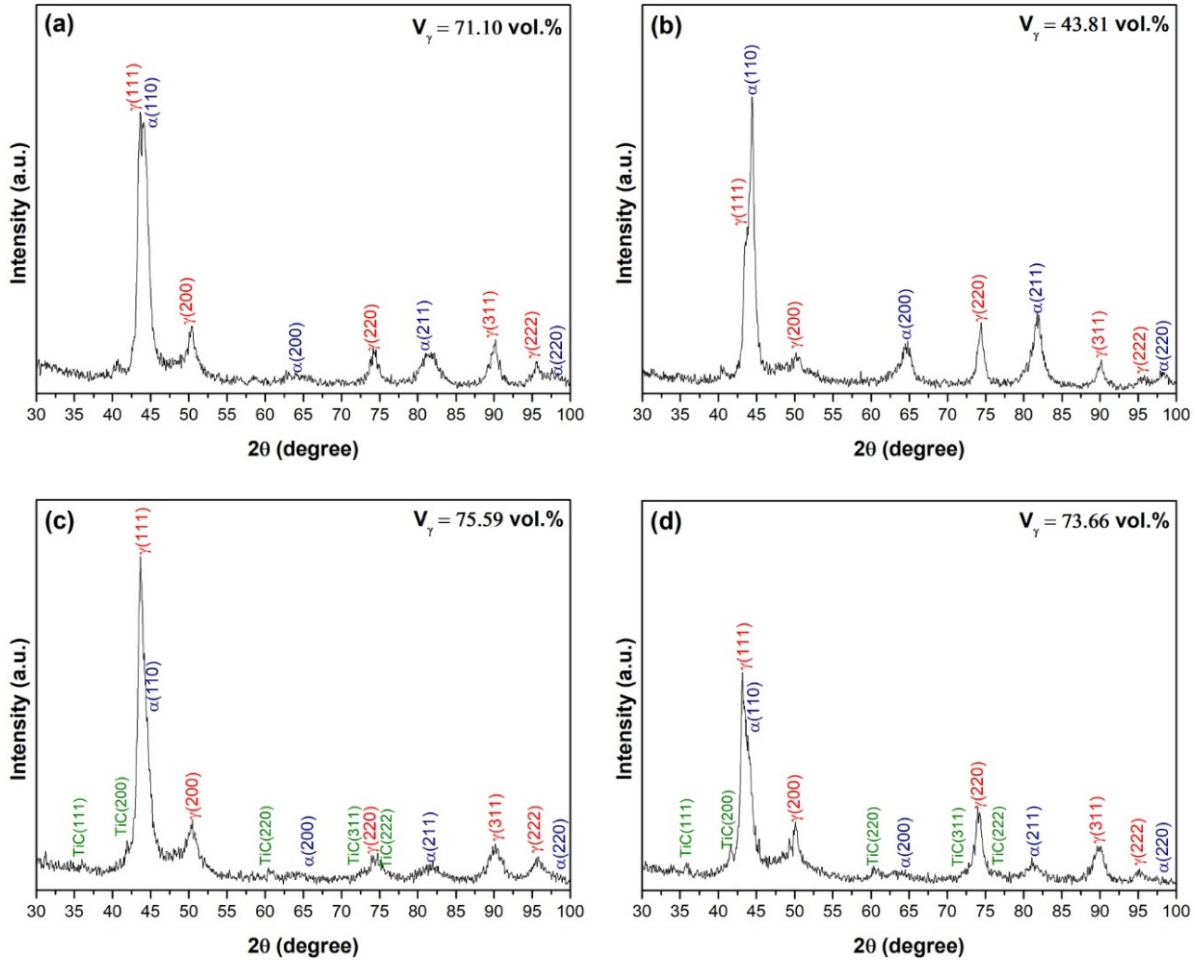

Fig. 2. XRD patterns of the (a) as-sintered and (b) deformed Fe-7%Mn specimens, (c) as-sintered and (d) deformed Fe-7%Mn-6%TiC specimens

After compressive deformation, about 27 vol.% of austenite decreased in the Fe-7%Mn specimen, whereas less than 2 vol.% of austenite decreased in the Fe-7%Mn-6%TiC specimen. The austenite transformed to strain-induced martensite due to plastic deformation, which was mainly controlled by austenite stability. The transformation kinetics of the strain-induced martensite became suppressed as austenite stability increased. It is believed that the addition of TiC thus played a role in increasing austenite stability in the Fe-7%Mn specimen. Fig. 3 shows the EBSD phase fraction maps for the Fe-7%Mn and Fe-7%Mn-6%TiC

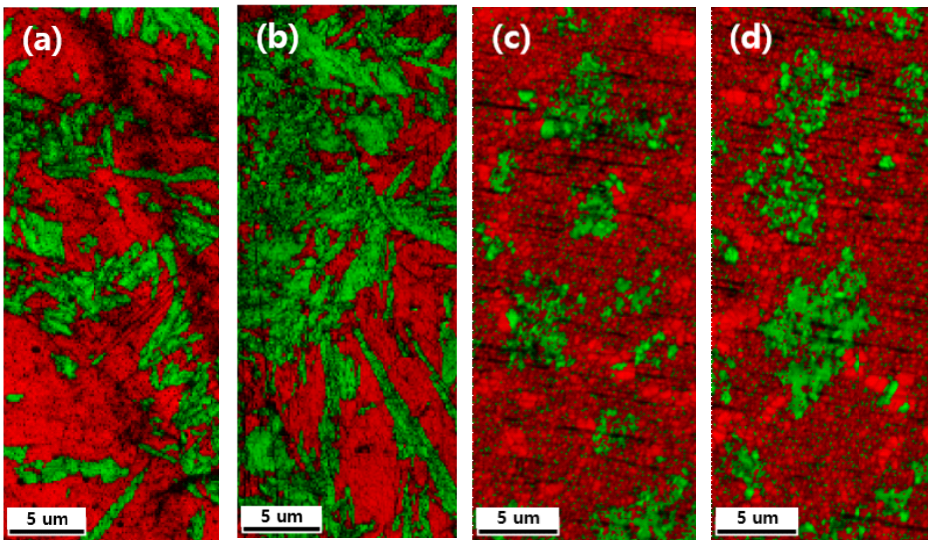

Fig. 3. EBSD phase fraction maps of the (a) as-sintered, (b) deformed Fe-7%Mn and (c) as-sintered, (d) deformed Fe-7%Mn-6%TiC (red: fcc austenite, green: bcc ferrite)

specimens. The austenite volume fraction of Fe-7%Mn and Fe-7%Mn-6%TiC in the as-sintered specimens were 70.0 and 78.7 vol.%, whereas that in the deformed specimens were 43.1 and 74.8 vol.%. This austenite volume fraction change matched closely with the values calculated from XRD analysis.

The effect of the TiC addition on the transformation kinetics of the strain-induced martensite was evaluated using the following model [24].

$$V_{\alpha'} = \frac{V_\gamma^0}{1 + \frac{p}{k_p \varepsilon^p V_\gamma^0}} \tag{3}$$

where $V_{\alpha'}$ is the volume fraction of strain-induced martensite, V_γ^0 is the initial volume fraction of austenite, k_p is the constant related to austenite stability, p is the autocatalytic strain exponent (= 2 for sintered Fe-Mn alloy [16]), and ε is the plastic strain. The higher the austenite stability, the lower the k_p value. The k_p values calculated for the Fe-7%Mn and Fe-7%Mn-6%TiC specimens were 88.0 and 4.5, respectively. This demonstrates that the TiC addition is effective in increasing austenite stability while also restricting the transformation kinetics of strain-induced martensite. The effect of the addition of TiC on the strain-induced martensite transformation kinetics was compared using Eq. (3), as shown in Fig. 4.

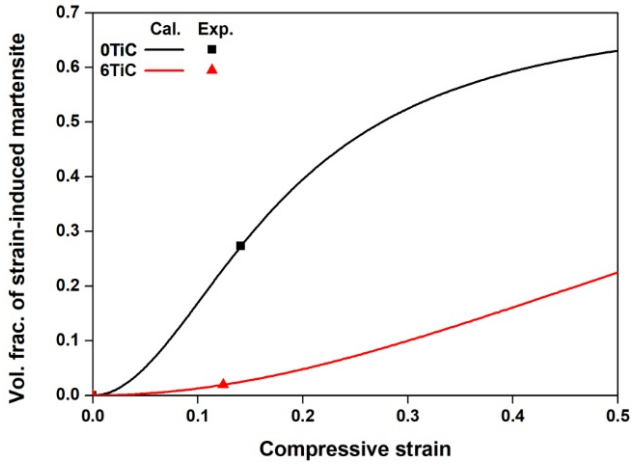

Fig. 4. Effect of TiC addition on strain-induced martensite transformation kinetics.

Fig. 5 shows the engineering stress-strain curves of the compressive specimens. The measured yield strength for the Fe-7%Mn and Fe-7%Mn-6%TiC specimens was 1133 MPa and 1818 MPa respectively. As expected, yield strength is increased by adding TiC. Regarding the strengthening mechanism, the constitutive equation to predict yield strength could be suggested as follows [25-29].

$$\sigma_{total} = \sigma_0 + \Delta\sigma_{gb} + \Delta\sigma_{dis} + \Delta\sigma_D \tag{3}$$

where σ_0 is the intrinsic strength, $\Delta\sigma_{gb}$ is the grain boundary strengthening, $\Delta\sigma_{dis}$ is the dislocation strengthening, and $\Delta\sigma_D$ is the dispersion strengthening. The σ_0 value of 100 MPa was used for medium manganese steel [30]. The grain boundary strengthening is based on the Hall-Petch relationship, given by

$$\Delta\sigma_{gb} = kd^{-1/2} \tag{4}$$

where k is the Hall-Petch slope (1370.25 MPa nm$^{-1/2}$ [31]) and d is the crystallite size (12 nm for Fe-7%Mn and 10 nm for Fe-7%Mn-6%TiC). The increment in dislocation density contributes to dislocation strengthening, as follows.

$$\Delta\sigma_{dis} = M\alpha Gb\rho^{1/2}, \quad \rho = \frac{3\sqrt{2\pi}\left(\varepsilon^2\right)^{1/2}}{Db} \tag{5}$$

where M is the Taylor factor (= 3.06 [32]), α is a constant (= 0.13), G is the shear modulus (= 81.6 GPa [30]), b is the Burger's vector (0.250 nm [32]), ρ is the dislocation density, ε is the micro-strain, and D is the crystallite size. ε and ρ were calculated using Eqs. (1) and (5). For the Fe-7%Mn-6%TiC specimen, dispersion strengthening by TiC addition should be considered.

$$\Delta\sigma_D = M\frac{0.4Gb}{\pi\lambda}\frac{\ln\left(\frac{2r'}{b}\right)}{\sqrt{1-\nu}},$$
$$\lambda = 2r'\left(\sqrt{\frac{\pi}{4f}} - 1\right), \quad r' = r\sqrt{2/3} \tag{6}$$

where λ is the edge-to-edge inter-precipitate spacing (= 156.7 nm), r' is the mean radius of a circular cross-section in a random plane for spherical precipitate (= 40.8 nm), ν is the Poisson ratio (= 0.295 [33]), f is the volume fraction of precipitate, and r is the mean precipitate radius. The volume fraction and mean radius of TiC particles were determined experimentally from TEM observation, as shown in Fig. 6. The volume fraction of TiC was roughly 0.09 and the average radius of TiC particles was 50 nm. The calculated yield strength by Eqs. (3)–(6) for the Fe-7%Mn and Fe-7%Mn-6%TiC specimens was 1113 MPa and 1800 MPa respectively. This prediction result shows strong consistency with the measured values. It should be noted that serrations were observed in the Fe-7%Mn specimen after plastic deformation began. It has been reported that serrations are related to the formation of strain-induced martensite in TRIP steels [34,35].

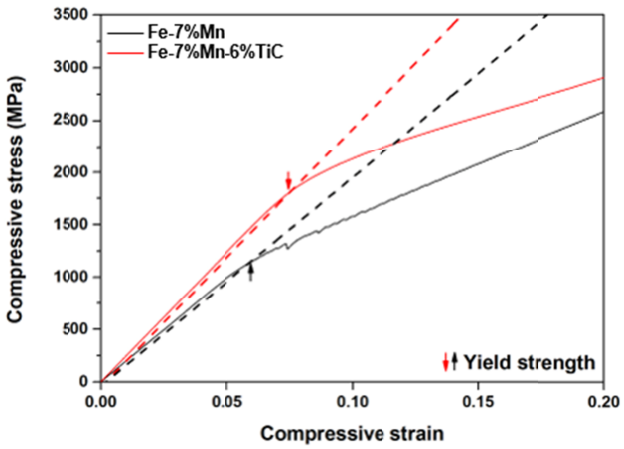

Fig. 5. Engineering compressive stress-strain curves of sintered specimens

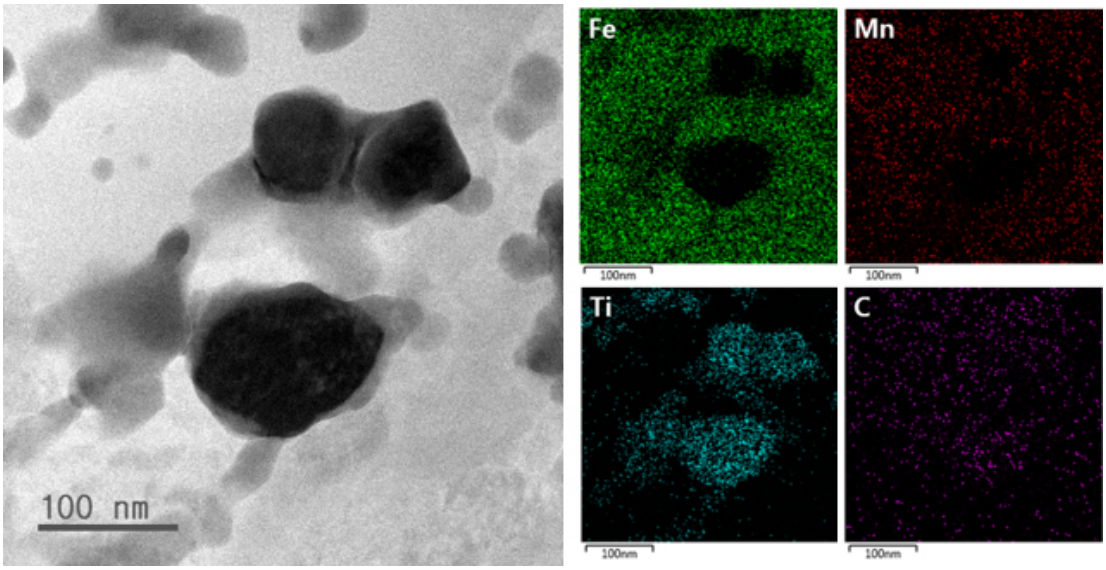

Fig. 6. TEM bright field image of sintered Fe-7Mn-6TiC composite

Fig. 7 shows the hardness change of the sintered specimens relative to changes austenite volume fraction. The Fe-7%Mn specimen's hardness increased with the deformation from 44.5 HRC to 54.7 HRC because a significant volume fraction of austenite was transformed to strain-induced martensite during deformation. On the other hand, the increment in hardness in the Fe-7%Mn-6%TiC specimen was only 0.7 HRC, because the volume fraction of strain-induced martensite formed during deformation was less than 2 vol.%.

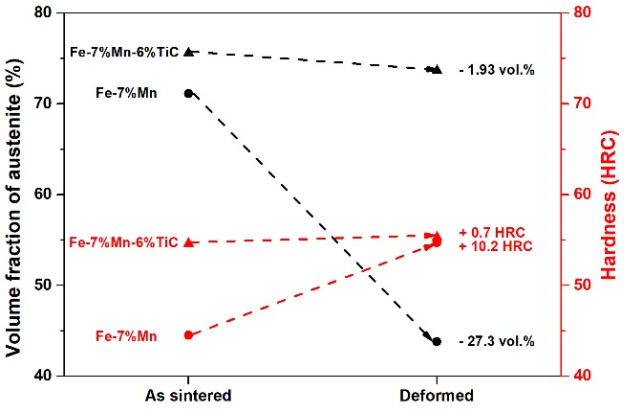

Fig. 7. Changes in relationship between hardness and austenite volume fraction due to deformation

4. Conclusions

In this study, we investigated the effect of the addition of TiC on strain-induced martensite transformation behavior and mechanical properties in a nanocrystalline Fe-7%Mn specimen fabricated by high energy ball milling and spark plasma sintering. The average size of crystallites was decreased by adding TiC to the alloy powders, resulting in an increased volume fraction of austenite at room temperature after SPS. The addition of TiC increased austenite stability, while strain-induced martensite transformation was correspondingly suppressed during deformation. A constitutive equation for predicting yield strength was proposed with regard to grain boundary strengthening, dislocation strengthening, and dispersion strengthening, and was closely consistent with experimental data. Due to the effect of TiC addition to the Fe-7%Mn-6%TiC specimen, both yield strength and hardness were higher than those in the Fe-7%Mn specimen; however, the lower austenite stability in the Fe-7%Mn specimen showed a marked improvement in mechanical properties through the formation of strain-induced martensite.

Acknowledgments

This research was supported by The Basic Science Research program through the National Research Foundation of Korea (NRF) funded by the Ministry of Education (2016R1A1B03935163) and "Research Base Construction Fund Support Program" funded by Chonbuk National University in 2019. Financial support was also provided by the Ministry of Trade, Industry and Energy (MOTIE) and the Korea Institute for Advancement of Technology (KIAT) through the International Cooperative R&D program (P006837).

REFERENCES

[1] Z. Yang, P. Mock, J. German, A. Bandivadekar, O. Lah, Transp. Res. Part D**6 4**, 53-69 (2018).

[2] M. Frondel, C.M. Schmidt, C. Vance, Transp. Res. Part A **45**, 1043-1051 (2011).

[3] N. Baluch, Z.M. Udin, C.S. Abdullah, Eng. Tech. Appl. Sci. Res. **4**, 686-689 (2014).

[4] D.K. Matlock, J.G. Speer, E.D. Moor, P.J. Gibbs, JESTECH **15**, 1-12 (2012).

[5] S.J. Lee, S. Lee, B.C. De Cooman, Scripta Mater. **64**, 649-652 (2011).
[6] K. Kim, S.J. Lee, Mater. Sci. Eng. A **698**, 183-190 (2017).
[7] M. Izumiyama, M. Tsuchiya, Y. Imai, J. Jpn. Inst. Met. 34, 291-295 (1970).
[8] S.J. Kim, C.G. Lee, T.H. Lee, C.S. Oh, Scripta Mater. **48**, 539-544 (2003).
[9] J. Wang, S. van Der Zwaag, Metall. Mater. Trans. A **32A**, 1527-1539 (2001).
[10] S.J. Lee, Y.K Lee, Mater. Sci. Forum **475-479**, 3169-3172 (2005).
[11] H.S. Yang, H.K.D.H. Bhadeshia, Scripta Mater. **60**, 493-495 (2009).
[12] K. Sugimoto, M. Misu, M. Kobayashi, H. Shirasawa, ISIJ Int. **33**, 775-782 (1993).
[13] E. Jimenez-Melero, N.H. van Dijk, L. Zhao, J. Sietsma, S.E. Offerman, J.P. Wright, S. van der Zwaag, Scripta Mater. **56**, 421-424 (2007).
[14] J.F. Breedis, Acta Mater. 13, 239-250 (1965).
[15] J. Mahieu, J. Maki, B.C. De Cooman, S. Claessens, Matall. Mater. Trans. A **33A**, 2573 (2002).
[16] S.J. Oh, D. Park, K. Kim, I.J. Shon, S.J. Lee, Mater. Sci. Eng. A **725**, 382-388 (2018).
[17] K. Kim, S.J. Oh, D. Park, I.J. Shon, S.J. Lee, Mater. Trans. **59**, 1206 (2018).
[18] S.J. Oh, I.J. Shon, S.J. Lee, J. Korean Powder Metall. Inst. **24**, 302 (2017).
[19] S.J. Oh, J. Jeon, I.J. Shon, S.J. Lee, Korean Powder Metall. Inst. **26**, 389-394 (2019).
[20] D. Park, S.J. Oh, I.J. Shon, S.J. Lee, Arch. Metall. Mater. **63**, 1477-1480 (2018).
[21] S.J. Oh, B.C. Kim, M.C. Suh, I.J. Shon, S.J. Lee, Arch. Metall. Mater. **64**, 863-867 (2019).
[22] C. Suryanarayana, M.G. Norton, X-ray Diffraction: A practical Approach, Plenum press, New York, 1998.
[23] ASTM E975-00, Standard Practice for X-Ray Determination of Retained Austenite in Steel with Near Random Crystallographic Orientation, vol. 03. 01, ASTM International, W. Conshohocken, PA, 2003.
[24] D. Yim, P. Sathiyamoorthi, S.J. Hong, H.S. Kim, J. Alloy. Compd. **781**, 389-396 (2019).
[25] H. Wen, T.D. Topping, D. Isheim, D.N. Seidman, E.J. Lavernia, Acta Mater. **61**, 2769-2782 (2013).
[26] P. Wang, H. Cai, S. Zhou, L. Xu, J. Alloy. Compd. **695**, 462-475 (2017).
[27] G. Dini, R. Ueji, A. Najafizadeh, S.M. Monir-Vaghefi, Mater. Sci. Eng. A **A527**, 2759 (2010).
[28] Y. Han, J. Shi, L. Xu, W.Q. Cao, H. Dong, Mater. Sci. Eng. A **530**, 643-651 (2011).
[29] S.J. Oh, J.H. Jun, M.H. Lee, I.J. Shon, S.J. Lee, Met. Mater. Int. **24**, 597-603 (2018).
[30] F. Yin, G.J. Cheng, R. Xu, K. Zhao, Q. Li, J. Jian, S. Hu, S. Sun, L. An, Q. Han, Scripta Mater. **155**, 26-31 (2018).
[31] M. Latypov, S. Shin, B.C. De Cooman, H.S. Kim, Acta Mater. **108**, 219-228 (2016).
[32] G. Zheng, Y. Chang, X. Li, C. Wang, H. Dong, IEEE, 661-665 (2018).
[33] L. Samek, E. De Moor, J. Penning, B.C. De Cooman, Metall. Mater. Trans. A **37A**, 109-124 (2006).
[34] Z.H. Cai, H. Ding, R.D.K. Misra, Z.Y. Ying, Acta Mater. **84**, 229-236 (2015).
[35] Z.C. Li, H. Ding, R.D.K. Misra, Z.H. Cai, Mater. Sci. Eng. A **682**, 211-219 (2017).